















## Nanostructured surface bioactive composite scaffold for filling of bone defects

Ciocca Leonardo <sup>1,\*</sup> , Lesci Isidoro Giorgio <sup>2</sup> , Ragazzini Sara <sup>3</sup> , Gioria Sabrina <sup>4</sup> , Valsesia Andrea <sup>5</sup> ,  
, Parrilli Annapaola <sup>6</sup> , Spadari Alessandro <sup>7</sup> , Dozza Barbara <sup>8</sup> , Mora Paolo <sup>9</sup> ,  
 Piattelli Adriano <sup>10</sup> , Iezzi Giovanna <sup>11</sup> , Tarsitano Achille <sup>12</sup> , Baldissara Paolo <sup>13</sup> 

<sup>1</sup>Researcher, professor of Oral and Maxillo-Facial Prosthodontics, Department of Biomedical and Neuromotor Science, Alma Mater Studiorum University of Bologna via S. Vitale 59 40125 Bologna Italy.

<sup>2</sup>Researcher in biochemical engineering of materials viale Firenze 235 48014, Castelbolognese, Italy.

<sup>3</sup>DDS, PhD, Department of Biomedical and Neuromotor Science, Alma Mater Studiorum University of Bologna via S. Vitale 59 40126 Bologna-Italy.

<sup>4</sup>Researcher, European Commission, Joint Research Centre (JRC), Directorate for Health, Consumers and Reference Materials, Via Enrico Fermi 2749, I-21027 Ispra (VA), Italy.

<sup>5</sup>Researcher, PhD, European Commission, Joint Research Centre (JRC), Directorate for Health, Consumers and Reference Materials, Via Enrico Fermi 2749, I-21027 Ispra (VA), Italy.

<sup>6</sup>PhD, MSc, Researcher, BITTA Laboratory, Rizzoli RIT Department, IRCCS - Istituto Ortopedico Rizzoli, Via di Barbiano 1/10, 40136, Bologna, Italy.

<sup>7</sup>Dean of Veterinary Surgery, Department of Veterinary Medicine, Alma Mater Studiorum University of Bologna Ozzano Emilia, Italy

<sup>8</sup>PhD, Rizzoli Laboratory Unit, Department of Biomedical and Neuromotor Sciences (DIBINEM), Alma Mater Studiorum University of Bologna, Via di Barbiano 1/10, 40136 Bologna, Italy.

<sup>9</sup>Technician, Department of Biomedical and Neuromotor Sciences, Alma Mater Studiorum University of Bologna, Via Pupilli 1, 40136 Bologna, Italy.

<sup>10</sup>MD, DDS, Dean and Professor of Oral Pathology and Medicine, Department of Medical, Oral and Biotechnological Sciences, University of Chieti; Chair of Biomaterials Engineering, Catholic University of San Antonio of Murcia (UCAM), Murcia, Spain; Villaserena Foundation for Research, Città Sant'Angelo (Pescara), Italy. via de' Vestini 31, 66100 Chieti, Italy.

<sup>11</sup>DDS, PhD, Researcher Department of Medical, Oral and Biotechnological Sciences, Department of Oral Sciences, University of Chieti via de' Vestini 31 66100 Chieti, Italy.

<sup>12</sup>Assistant Professor of Maxillofacial Surgery, Maxillofacial Surgery Unit, S. Orsola-Malpighi Hospital, Department of Biomedical and Neuromotor Sciences, (Head Prof. Claudio Marchetti), Via Massarenti 9 40100 Bologna Italy.

<sup>13</sup>Researcher, Aggregate professor of Dental Material, Department of Biomedical and Neuromotor Science, Alma Mater Studiorum University of Bologna via S. Vitale 59 40126 Bologna-Italy.

\*corresponding author e-mail address: [leonardo.ciocca@unibo.it](mailto:leonardo.ciocca@unibo.it) | Scopus ID [660305552](https://orcid.org/0000-0002-6603-0552)

## ABSTRACT

The aim of this study was to investigate the chemical and physical surface properties of a hybrid nano-hydroxyapatite/collagen/polycaprolactone (nHA/Coll/PCL) material, and to test its *in vitro* biocompatibility and *in vivo* osteointegration. Mineralized collagen fibers with nHA were admixed with PCL at a weight proportion of 50:50. The material was characterized by transmission X-ray diffraction (XRD), electron microscopy (TEM), atomic force microscopy (AFM), force spectroscopy, X-ray Photoemission Spectroscopy (XPS), and biocompatibility testing using human mesenchymal stem cells (MSCs), and Hepatocyte carcinoma (HePG2) and primary osteogenic sarcoma (SAOS-2) cells as complementary tests. In addition, the ability of this material to fill three-wall bony defects was tested in the mandible of a sheep. The material had confirmed the relative low crystallinity of the HA having a nano-sized dimension, which was composed of only oxygen, carbon, calcium and phosphorus, without no residual cytotoxic element. Human MSCs on the surface scaffold showed high metabolic activity and a high rate of viability. Biocompatibility complementary testing using HePG2 and SAOS-2 cells showed good metabolic activity, and the lactate dehydrogenase assay using HePG2 cells demonstrated no significant cytotoxicity. Histological analysis of the in-vivo experimentation showed osteointegration of the material and the absence of inflammatory cells at the bone-scaffold interface. Some areas showed bone-cell seeding and isolated agglomerates of bone cells were evident in the inner scaffold.

**Keywords:** bone substitute; bioactive surface; hybrid scaffold; nanohydroxyapatite; osseointegration; regenerative medicine.

## 1. INTRODUCTION

After cancer removal, trauma, or infection, residual bone defects are a challenge for reconstructive surgery: maxillofacial bone deficiencies frequently need to be restored using bone substitutes that mimic the original esthetic appearance and allow recovery of the missing anatomy. A variety of non-resorbable and resorbable bone substitutes have been used to restore the anatomy and function of the mandibular and maxillary bones; e.g., natural (such as the autologous free vascularized flap), allogenic, or synthetic grafts. Moreover, artificial bioengineered materials are used for non-resorbable scaffolds; although, to date, no such material has shown features similar to autologous grafts. For this reason, new materials with enhanced biocompatibility and osteointegration have been bioengineered [1-4]. The structure of a tissue-engineering scaffold determines its bioactivity and

osteoinductive ability [5]. Micropore size, porosity, and interconnectivity are reportedly directly related to bone mineralization and vascularization. Also, the properties of the surface with which the cells interact is an important consideration, as well as is the interconnected porous structure, which enables cell proliferation and bestows on the scaffold good mechanical properties [6]. The ideal tissue-engineering scaffold should act as a surrogate for the native extracellular matrix (ECM), comprise proteins (mainly collagen, Coll) and polysaccharides, and possess three-dimensional (3D) nanometer-scale hierarchical fibrous structures [7-10]. Therefore, tissue-engineering scaffolds can be engineered by fabricating protein-polysaccharide composite nanofibers. Scaffolds with both micro- and nano-scale structures promote cell growth and new tissue formation [3,11]. Scaffolds

should have a large surface area and high porosity to facilitate cell attachment and nutrient diffusion [12]. The design of tissue-engineering scaffolds has to take into consideration the vasculature and perfusion permissiveness of the scaffold, which fundamentally enhances cell viability.

Nano-hydroxyapatite (nHA), which is composed of the same ions as the major mineral constituent of bone, is an attractive implant material for bone regeneration due to its biocompatibility and osteoconductivity properties. Furthermore, it does not cause systemic toxicity or immunological reactions [13-15]. Porous HA scaffolds are used in bone-tissue engineering, as their architecture mimics very closely that of the bone extracellular matrix (bECM), thereby providing a favorable environment for biological processes [16-17]. This requires highly interconnected macro- and micro-porous networks. The size of the granules and porosity of HA are its most important characteristics. Indeed, nanometer grains and a high surface porosity increase osteoblast adhesion, proliferation and differentiation, and so facilitate osteointegration [13].

## 2. MATERIALS AND METHODS

### 2.1. Synthesis of biomimetic nHA/Coll.

H<sub>3</sub>PO<sub>4</sub> (85% purity), Ca(OH)<sub>2</sub> (96% purity), NaOH, PCL (average molecular weight [Mw] 14,000 Da), ethanol (98%), dichloromethane, and powdered Coll fibers from bovine Achilles tendon were purchased from Sigma-Aldrich (Milan, Italy). Briefly, H<sub>3</sub>PO<sub>4</sub> (1.26 M) and Ca(OH)<sub>2</sub> (1.35 M) solutions were prepared in ultrapure water. Then, 180 mL of H<sub>3</sub>PO<sub>4</sub> (1.26 M) was added to 0.3 g of Coll fibers and blended; next, 300 mL of Ca(OH)<sub>2</sub> (1.35 M) was added to the mixture dropwise using a dropping funnel. The temperature was monitored from the beginning (0–1.5°C) to the end (7°C) of the reaction, which was blended overnight at 4°C. Subsequently, NaOH (2 M) was added to adjust the pH to 12. The suspension was centrifuged at 7,000 rpm and washed three times with ultrapure water to eliminate unreacted particles. The sample was lyophilized at –48°C and 0.052 bar for 24h.

### 2.2. Preparation of scaffold.

Biomimetic nHA/Coll, after grinding, was admixed with PCL, previously dissolved in dichloromethane using ultrasound, in the weight proportion PCL:nHA/Coll 50:50, and a custom computer-aided design and manufacture (CAD-CAM) mold was filled with the nHA-Coll/PCL mixture to obtain the final volume of the scaffold. The scaffold was incubated at 25°C and 1 atm for 24 h to allow the solvent to evaporate through the pores of the mold, thus creating interconnected and homogeneously distributed pores. Scaffolds were washed in pure ethanol to remove traces of solvent and dried under vacuum for 2 h.

### 2.3. Sample preparation.

For *in vitro* chemical and physical characterization, nHA-Coll-PCL three forms of the samples were prepared as follows. Powder samples of nHA-Coll and nHA-Coll-PCL were subjected to X-ray Photoemission Spectroscopy (XPS), transmission electron microscopy (TEM) and BET analysis. Drop coating samples for X-ray diffraction (XRD) were prepared by drop coating after dispersing the powder in dichloromethane. A

In this study, a hybrid nano-hydroxyapatite/collagen/polycaprolactone (nHA/Coll/PCL) composite material was structurally modified compared to previously composite material tested by authors in another publication [18]. The main purpose of this study was to improve the hydrophilic property of the scaffold and the bioactivity of the surface by modifying the Ca/P ratio of its nanostructured surface. It had been proposed that the upper surface layer of HA (Ca/P ratio 1,67) should be reduced to increase the bioactivity of the surface [19]. However, a bioactive surface with a Ca/P ratio of less than 1 is not suitable for implantation into the body because of its high solubility and acidity [20]. The proposed biomimetic scaffold has an altered PCL/nHA-Coll ratio, which enables its use to fill three-wall bony defects, gaining the osteointegration with the surrounding bone and producing no adverse reaction during healing. *In vitro*, we investigated the chemical and physical surface properties of the nHA/Coll/PCL material, as well as its biocompatibility and, as a proof of principle, *in vivo* osteointegration in a three-wall bony defect of the sheep mandible.

film was formed after evaporation of the solvent at room temperature (RT).

Tablet samples of nHA-Coll and nHA-Coll-PCL were produced from 200 mg of powder using 2 tons of pressure for 60 s in a hydraulic manual press with a stainless-steel mold (Graseby Specac, Orpington, UK). The tablets were 13 mm in diameter and approximately 3 mm in thickness and appeared compact and homogeneous. Tablets were subjected to atomic force microscopy (AFM), force spectroscopy, and biocompatibility testing.

### 2.4. Material characterization and biocompatibility tests.

#### 2.4.1. TEM.

Two powder samples (n-HA/coll and n-HA/coll/PCL) were prepared by blotting a 3 µL drop of powder suspended in Milli-Q water after being sonicated for 15 min using Vial Tweeter (Hielscher Ultrasonics GmbH, Teltow, Germany). Samples were dried in a desiccator overnight and negatively stained with uranyl acetate (5% w/v) for 10 s or Uranyl Less™ solution for 1 min. Images were acquired using a JEM-2100 (JEOL, Tokyo, Japan) high-resolution TEM (HR-TEM) at 120 kV. Elemental analysis was performed in TEM mode at 120 kV by energy-dispersive X-ray spectroscopy (EDS) using the X-Flash Detector 5030 (Bruker, Milan, Italy) coupled to the TEM.

#### 2.4.2. X-Ray diffraction.

The samples (n-HA/coll and n-HA/coll/PCL) were prepared using the drop-coating technique. The XRD spectra were acquired in standard theta-2 theta mode and glancing angle mode (6°).

#### 2.4.3. AFM and force spectroscopy.

To describe the surface morphology, the AFM images of tablets were acquired using a Solver instrument (NT-MDT, Zelenograd, Russia) with parameters set at scan sizes of 50, 10, and 2 µm<sup>2</sup> in tapping (intermittent contact) mode using a standard silicon cantilever (NT-MDT) with a force constant (k) of 10.86 N/m and a nominal tip radius of 10 nm.

**2.4.4. Brunauer-Emmet-Teller Surface Area Analysis.** The experiments were carried out on nHA-Coll in powder form. The

measurement foresees a heating step to degas the sample at above 100°C.

#### 2.4.5. X-ray Photoemission Spectroscopy (XPS).

XPS measurements were performed in an Axis Ultra DLD spectrometer (Kratos, Manchester, UK), using a  $K\alpha$  Al monochromatic source ( $h\nu=1486.6$  eV) operating at 150 W and X-ray spot size of  $400\times700\ \mu\text{m}^2$  in hybrid mode. The residual pressure of the analysis chamber during the analysis was less than  $8\times10^{-9}$  Torr. For each sample, both survey spectra (0–1150 eV, pass energy 160 eV) and high-resolution spectra (pass energy at 20 eV) were recorded. The surface charge was compensated by a magnetic charge compensation system and the energy scale was calibrated by setting the C 1s hydrocarbon peak to 285 eV and the Au4f7/2 at 84.00 eV. The take-off angle for the acquisitions was 90° with respect to the sample surface. The data were processed using Vision2 software (Kratos Analytical, UK) and the analysis of the XPS peaks was carried out using a commercial software package (Casa XPS v2.3.18PR1, Casa Software Ltd., UK). Peak fitting was performed with no preliminary smoothing. Symmetric Gaussian–Lorentzian product functions were employed to approximate the line shapes of the fitting components after a Tougaard type background subtraction.

#### 2.5. In-vitro biocompatibility.

##### 2.5.1. Isolation and culture of bone marrow-derived mesenchymal stem cells (MSCs).

Human MSCs were isolated from bone marrow samples from the iliac crest of subjects undergoing surgery at Rizzoli Orthopaedic Institute (Bologna, Italy) after obtaining informed consent. Cells were isolated and cultured as described previously [21]. Briefly, nucleated cells were isolated in a density gradient solution (Ficoll-Paque Premium; GE Healthcare, Uppsala, Sweden) and cells capable of adhering to plastic were selected. MSCs were cultured in  $\alpha$ -modified minimum essential medium ( $\alpha$ -MEM; BioWhittaker, Lonza, Verviers, Belgium) supplemented with 20% lot-selected fetal bovine serum (FBS; Lonza) and 1% GlutaMAX™ (Invitrogen, Paisley, UK). The medium was changed every 3–4 days.

##### 2.5.2. MSC seeding and culture of cell-seeded scaffolds.

Before cell seeding, three independent nHA-Coll-PCL scaffolds were rinsed with phosphate-buffered saline (PBS) and incubated with culture medium ( $\alpha$ -MEM; BioWhittaker, Lonza, Verviers, Belgium) overnight at 37°C in a 5% CO<sub>2</sub> atmosphere. The scaffolds were dried on filter paper and transferred to 48-well non-treated plates. Next, 125,000 MSCs were suspended in 10  $\mu\text{L}$  of culture medium, and the resulting cell suspension was slowly dropped onto the top surface of the scaffold. The cells were incubated for 3 h (37°C, 5% CO<sub>2</sub>) to allow attachment to the scaffold. Subsequently, to cover the scaffold, 1 mL of culture medium was slowly added by pipetting down the side of the well. The plates were returned to the incubator and incubated for 1, 3, or 7 days under static culture conditions.

##### 2.5.3. Evaluation of cell seeded scaffolds.

Cell viability was assessed using a Live/Dead® Viability/Cytotoxicity Kit (Invitrogen) according to the manufacturer's instructions. Green-fluorescent calcein-AM was used to detect intracellular esterase activity, and red-fluorescent EthD-1 to stain dead cells. Samples were observed under a

fluorescence microscope (Eclipse TE2000-U; Nikon, Tokyo, Japan) equipped with a Nikon DS-Vi1-U3 charge-coupled device (CCD) digital camera.

The metabolic activity of cells on the scaffolds was evaluated 1, 3, and 7 days after seeding by nontoxic Alamar Blue (AB) assay. AB solution (AbD Serotec, Oxford, UK) was prepared by diluting 1 mL of AB reagent in 10 mL of culture medium [22]. The constructs were transferred to a new 48-well plate containing 0.6 mL/well of AB solution. After incubation for 4 h, the fluorescence of 100  $\mu\text{L}$  aliquots was measured in triplicate using a microplate fluorometer (Bio-Tek Instruments Inc., Winooski, VT, USA) at an emission wavelength of 590 nm and an excitation wavelength of 530 nm. The intensity of the fluorescence signal was expressed in arbitrary fluorescence units. A blank value was measured under identical conditions but without cells, and was subtracted from the construct values to obtain the fluorescence signal originating from the cellular activity.

#### 2.5.4. Biocompatibility: complementary test.

**2.5.4.1. Sample preparation.** Two different tablets (n-HA/coll and n-HA/coll/PCL) were sterilized by washing three times with EtOH, and rinsed three times with PBS (Invitrogen). Hepatocyte carcinoma (HePG2) cells (HB-8065™ ATCC; LGC Standards, Wesel, Germany), or Primary osteogenic sarcoma (SAOS-2) cells (300331; CLS, Eppelheim, Germany) (N = 500,000) were used as a complementary test and were seeded on the tablets at the bottom of wells of a 24-well Falcon plate (Fig. 1).

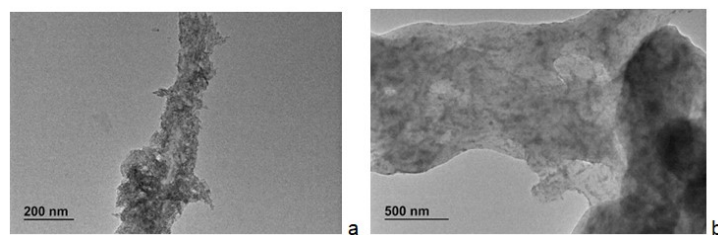


**Figure 1.** TEM images of nanocrystals of HA covering the collagen fibres (a) and completely enveloped by PCL (b).

HePG2 and SAOS-2 cells were cultured in the RPMI-1640 (Invitrogen) and Ham's F12 (Invitrogen) cell culture, respectively, both complemented with 10% Fetal bovine serum (FBS) (F-7524; Sigma), 2 mM L-glutamine, 100 U/mL and penicillin-streptomycin (Invitrogen). After 24 or 72 h, medium was removed and the cells were fixed with 10% paraformaldehyde for 20 min and washed three times with PBS. Cells were stained with phalloidin-488 (Invitrogen) (1:100 in PBS) for 40 min at 37°C. Nuclei were counterstained with Hoechst 1:1,000 in PBS, and images were acquired using an Axiovert microscope (Zeiss, Oberkochen, Germany).

**2.5.4.2. Lactate dehydrogenase (LDH) cytotoxicity assay.** HePG2 cells were used to assess the cytotoxicity of nHA-Coll and nHA-Coll-PCL powder (HB-8065™ ATCC; LGC Standards), in accordance with ISO 10993-5:2009 and Standard Test Method for Evaluation of Cytotoxicity of Nanoparticulate Materials in Porcine Kidney Cells and Human Hepatocarcinoma Cells (ASTM E2526-08). Briefly, 50,000 cells were cultured on the bottom of wells of standard 96-well Falcon plates for 24 h in 200  $\mu\text{L}$  of RPMI-1640 (Invitrogen) supplemented with 10% FBS (F-7524; Sigma), 2 mM

L-glutamine, and 100 U/mL penicillin-streptomycin (Invitrogen). Next, the medium was removed and replaced with medium containing up to 50 mg/mL nHA-Coll-PCL. Cytotoxicity was evaluated after 24 h using the BioVision LDH Cytotoxicity Assay Kit (K311-400). Next, 150  $\mu$ L of medium was removed from each well and transferred to another 96-well plate. After centrifugation at 1,000 g for 5 min to remove particulates, 100  $\mu$ L of the supernatant was transferred to a new plate. One hundred microliters of reaction mixture (prepared according to the manufacturer's instructions) were added to each well and incubated for 20 min in the dark at RT. The plate was read in a multiplate reader (EnSpire; PerkinElmer, Waltham, MA, USA) at 490 nm with a reference wavelength of 680 nm. Negative control, positive control (0.1% TritonX-100) and Digitonin (30  $\mu$ g/mL) as an internal control were assayed, and three replicates were performed per condition.

## **2.6. Scaffold and bone-plate customization.**

Scaffold molding and bone-plate manufacturing were described previously [18]. Briefly, after generating a 3D model of a sheep skull from computed tomography (CT) scans, the mandibular corpus was virtually resected from the model to artificially create a three-wall bony defect in the sub-molar area. We manufactured a mold for a scaffold with the same volume as the bone to be ablated. According to this volume, a bone plate was designed and manufactured to contain and stabilize the bone substitute during healing. Also, a resin surgical guide was designed and manufactured according to the volume of the scaffold to guide bone cutting.

## **2.7. In-vivo pilot study.**

### **2.7.1. Surgery.**

The study plan was independently reviewed and approved by the Ethics Board of the National Institute of Health (no. 781/2015-PR). The surgical technique was as in a previous study [18]. Briefly, a defect was created in the sub-molar area using a surgical guide designed to reproduce a three-wall bony defect. An oscillating saw was used to resect the bone and insert the scaffold connected to the bone plate, which was screwed to the bone using the same guide holes used to position the surgical guide. This enabled accurate and precise insertion of the scaffold, with no gap between the scaffold and the bone defect.

The sheep were housed at the Department of Veterinary Medical Sciences for 16 weeks. Postoperative treatment was procaine penicillin 20,000 U/kg/SID IM and gentamicin 6.6 mg/kg/SID IM for 5 days, followed by flunixin meglumine 2.2 mg/kg/SID IM for 3 days. At the 4-month follow-up, two oral implants (3.8  $\times$  11 mm, Kono TTI; Sweden and Martina, Padua, Italy) were inserted in the scaffold volume using the same anesthetic and

pharmacologic procedure. The sheep were euthanized by IV injection of ketamine (5 mg/kg, IM), midazolam (0.4 mg/kg, IM), and embutramide (70 mg/kg) plus mebezony (TanaxVR; 15 mg/kg), and an explant was harvested from the mandible for histological examination.

### **2.7.2. Micro-CT.**

As described previously,[18] the explanted specimen was scanned using a high-resolution micro-CT instrument (SkyScan 1176; Bruker-microCT, Kontich, Belgium) fitted with a copper filter 0.1 mm in thickness, at a power setting of 278  $\mu$ A and a source voltage of 70 kV. Scan images (668  $\times$  1,968 pixels) had a nominal resolution of 35  $\mu$ m (pixel size) and were recomposed using NRecon software (ver. 1.6.8.0; Bruker-MicroCT) to obtain microtomographic sections (1,968  $\times$  1,968 pixels) with the original nominal resolution. Correction factors for beam hardening and ring artifacts were applied using NRecon relative tools after specific relative alignment of each scan.

### **2.7.3. Histological analysis.**

The specimens were immersed in formalin and cut into three pieces using a precision saw. We have distinguished three different parts, distal, medial and proximal, and performed different sections. The proximal and distal were made front cuts, while the medial piece has been sectioned in the axial direction. In order to conduct an accurate histological analysis, five representative histological sections were obtained from each sample. The retrieved specimen was immediately stored in 10% buffered formalin and processed to obtain thin ground sections using the Precise 1 Automated System (Assing, Rome, Italy) [23]. The specimens were dehydrated in a graded series of ethanol rinses and embedded in a glycolmethacrylate resin (Technovit 7200 VLC, Kulzer, Wehrheim, Germany). After polymerization, the specimens were sectioned, with a high precision diamond disk at about 150  $\mu$ m and ground down to about 30  $\mu$ m with a specially designed grinding machine Precise 1 Automated System. Three slides were obtained from each specimen, subsequently stained with acid fuchsin and toluidine blue before the analysis.

Histological images were captured using a light microscope (Laborlux S, Leitz, Wetzlar, Germany) connected to a high-resolution video camera (3CCD, JVCKY-F55B, JVC, Yokohama, Japan) and interfaced with a monitor and PC (Intel Pentium III 1200 MMX, Intel, Santa Clara, CA, USA). This optical system was associated with a digitizing pad (Matrix Vision GmbH, Oppenweiler, Germany) and a histomorphometry software package with image capturing capabilities (Image-Pro Plus 4.5, Media Cybernetics Inc., Immagini & Computer Snc, Milano, Italy).

## **3. RESULTS**

### **3.1. In vitro.**

#### **3.1.1. Material characterization.**

Bone tissue engineering for maxillofacial reconstruction of residual defects after cancer, trauma, or infective injury makes use of diverse resorbable and non-resorbable materials. The scaffolds engineered for reconstruction of the maxillofacial skeleton are typical of natural or synthetic biocompatible materials, such as HA, calcium phosphate ceramics, Coll, polymers, bioglass,

cements, and bioactive glass ceramics [24-33]. As in orthopedic surgery, several commercial alternatives for reconstructive maxillofacial surgery are available too, each of which has advantages and limitations in terms of biocompatibility, osteointegration, and immunogenicity. In this study, a new composite material with the same biomimetic properties as our prior works [34-35,37-39,42-44] but with the ability to function as a filler, was evaluated. To this end, the PCL concentration was



reduced from 60% to 50% to increase the nHA on the surface area and so improving osteointegration ad adhesion of the cells due to the increased hydrophilicity and the surface bioactivity. The new nHA-Coll-PCL composite material was created to develop a customized scaffold to restore residual bony defects, in the skeleton as in the facial skull, after cancer surgery, or to correct anatomy altered by congenital defects or traumatic injuries. TEM showed the polydispersity and discontinuity of the film formed by spin coating. Higher-magnification images showed small nanoparticles (36 nm). The powder had a size distribution of 30–140 nm (Fig. 1a), and some collagen bands were visible after negative staining. PCL was also visible, showing the nHA/collagen distribution inside matrix and completely enveloping it (Fig. 1b). Elemental analysis carried out by EDX detected in the composite material showed the presence of only O, C, Ca, and P (Fig. 2).

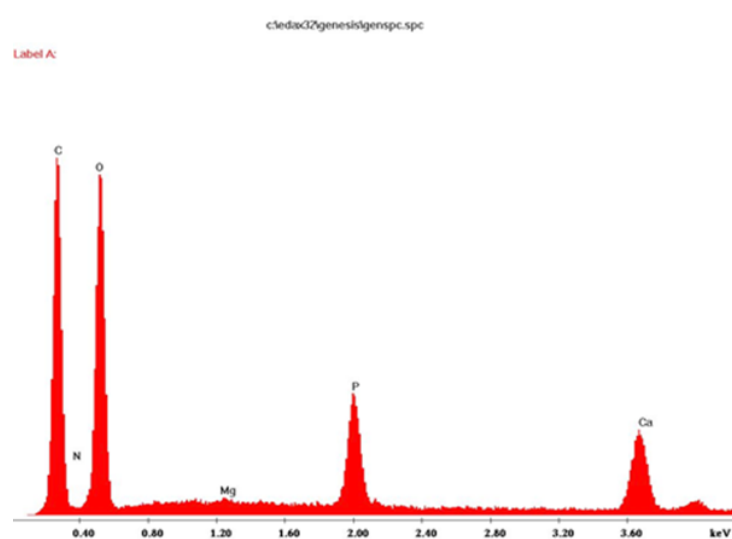


Figure 2. EDX spectra of HA-PCL sample.

The XRD spectra confirmed the relative low crystallinity of the biomimetic nano HA due the presence of the amorphous phase like collagen as it happens in biogenic bone. AFM image confirmed the homogeneous distribution of the nanostructure and collagen fibers on the surface of the tablet showing a higher force adhesion of the silicon tip (from the cantilever) on the tablet containing HA-coll respect to HA alone. AFM at a scan size of 2  $\mu\text{m}$  (Fig 3a) showed homogeneous agglomeration of grains, the size of which was in accordance with that determined by TEM. At a scan size of 50  $\mu\text{m}$  (Fig 3b), the surface showed elongated structures, which are likely to be collagen fibers. The surface roughness values of the material are listed in Table 1.

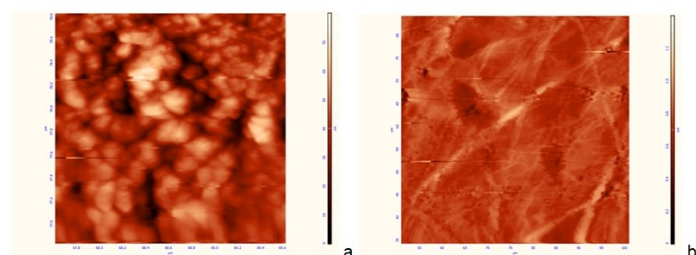


Figure 3. AFM images acquired on the tablets at a scan size of 2  $\mu\text{m}$  (a) and at a scan size 50  $\mu\text{m}$  (b).

Table 1. Root-mean-square values for the roughness of the two samples at the different length scales.

	HA Roughness (nm)	HA-PCL Roughness (nm)
2 $\mu\text{m}$	14	15
10 $\mu\text{m}$	38	43
50 $\mu\text{m}$	127	179

The same cantilever was used to perform force spectroscopy on the two samples. Briefly, the tip is brought into contact with the surface by the piezo electric driver, then is pushed against the surface for about 500 nm, this part of the curve is called “approach curve”. Then the tip is retracted from the surface and ends in a position of no interaction, in the specific retract curve. The result of 100 averaged curves is shown in Figure 4.

From the approach curve, using a silicon chip as reference of a perfectly rigid material, it's possible to measure the elastic modulus of the materials. The displacement difference between silicon and HA (or HA-PCL) is the amount of material that is indented by the tip. By using a Hertzian model it is possible to estimate the Young modulus for the HA tablet, which is calculated to be 0.4 GPa. This value is much lower than the one reported in the literature for the HA (of about 80 GPa) and for the collagen (5 GPa), meaning that the indentation is probably due to the displacement of the grains structure in the tablet, making the material brittle than expected. From the retract curve it is possible to observe if the tip and the material show adhesion. The force of adhesion is directly measured using the force constant of the cantilever. As shown by Figure 4, the adhesion between the Silicon tip and the HA-PCL is much larger ( $437 \pm \text{nN}$  against  $87 \pm \text{nN}$ ) than the one measured on the HA. The result from BET analysis on HA-coll showed a value of the surface area of  $127.27 \text{ m}^2/\text{g}$ .

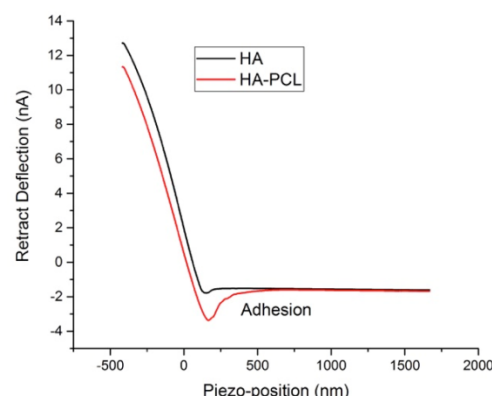
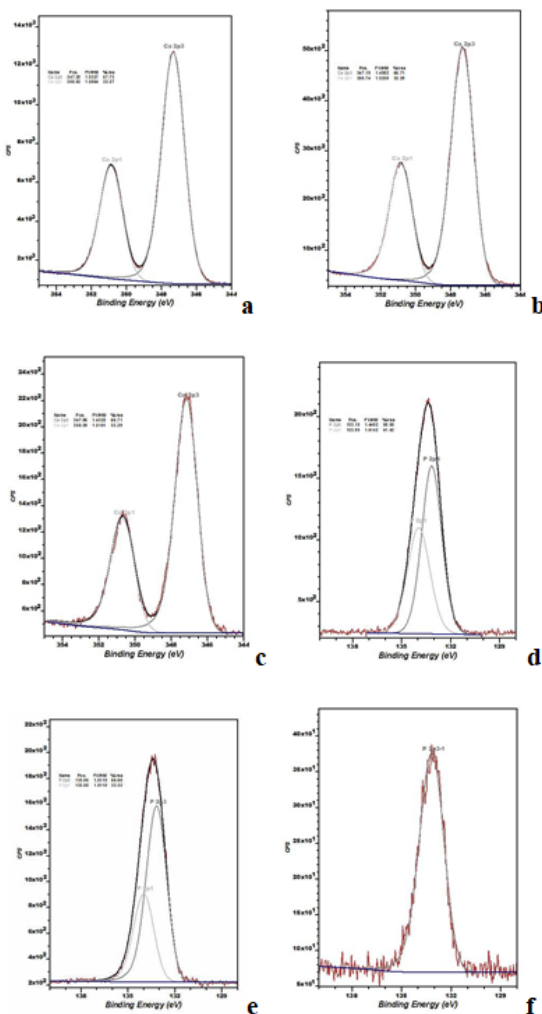


Figure 4. Average of 100 approach and retract curves for the HA and the HA-PCL samples.

The modification of the surface of the new scaffold HA-coll-PCL, in term of Ca/P ratio and binding energy, were showed by XPS analysis suggesting an improved hydrophilicity and bioactivity of the scaffold surface. The surface chemical compositions of the HA samples are presented in Table 2. XPS analysis of sample nHA-coll, revealed that the ratio Ca/P was 1.67, making it the same matching to stoichiometric value of an ideal phase pure HA, whilst it was observed that in surface of HA-coll-PCL, the Ca/P molar ratio diminished to ca. 1.46 probably due to the addition of organic modifiers (Table 2). This clearly

suggests that some of the ligands are replacing near surface inorganic phosphates. On the other hand, the presence of collagen was not detected probably because of the low amount of the collagen fibers (about 0.1% in weight) and the localized accumulation of the collagen fibers as identified by the TEM analysis. This conclusion is supported by Time of Flight Secondary Ion Mass Spectrometry (ToF-SIMS) analysis in which, despite of the high sensitivity, the presence of collagen was not detected (data not shown). The deconvoluted spectra for Ca and P, recorded on HA, HA-coll and HA-coll-PCL samples are presented in Figure 5.

The Ca2p spectrum of bare HA shows the Ca 2p<sub>3/2</sub> peak at 347.28eV with a spin-orbit splitting of 3,54eV. (Fig. 5 a,b,c) The P2p peak of the Ha and HA-coll can also be deconvoluted into two peaks, with binding energy and spin-orbit splitting of 133 eV and 0.8 eV, respectively [36-39] (Fig. 5 d,e,f). The slight decreased binding energy of Ca 2p and P 2p, when HA-coll was mixed to PCL, suggest that a HA surface properties modification was due to the functionalization of its surface by polymers. Analysis of the C1s specimen (Fig. 6 a,b) and O1s specimen (fig. 6 c,d) core level spectra of the HA-coll-PCL samples confirms the surface modification. In particular, while the C1s specimen envelope of the bare, HA sample shows the presence of three components (at about 285eV, 286.5 and 289.4eV) that can be attributed to hydrocarbon, hydroxyl and carboxylate groups related to surface contamination.



**Figure 5.** Ca 2p and P2p core level spectra of HA [(a) and (d)]; HA-coll [(b) and (e)]; HA-coll-PCL [(c) and (f)].

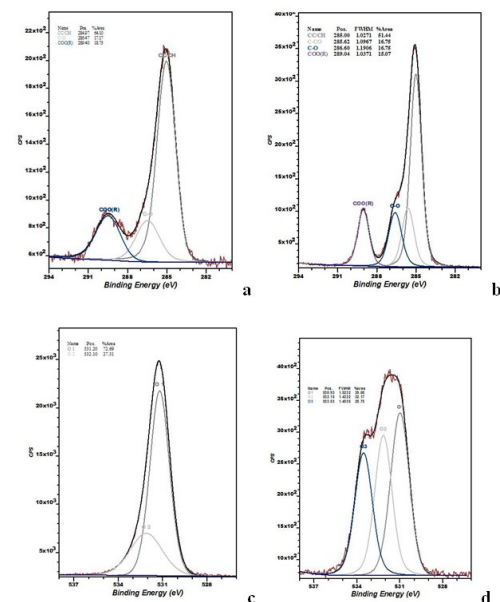


**Figure 6.** C1s and O1s specimens core level spectra of: HA (a) and (c); HA-coll-PCL (b) and (d).

After the PCL functionalization, the C1s specimen envelope changes shape and shows a clearer separation between the different components (Fig. 6b). The four components are at 285, 285.6, 286.5 and 289 eV, respectively. Both energy position and peak shape are well in agreement with the published spectra of pure PCL films.[40] The O1s specimen core level spectra illustrated in figure 6 (c,d) also supports this finding. In particular O1s envelope of HA bare sample shows a major component at about 531.2eV attributable to the PO bonding and a minor at about 532eV related to C-O moieties.[41] After the surface modification with PCL the third component at about 533.5eV typical of C-O bond in PCL is observed. Moreover, the component related to the P-O moieties is slightly shifted toward lower binding energy (about 530.5eV) indicating a possible distortion of the HA structure.

### 3.1.2. Biocompatibility: human MSCs and HePG2/SAOS-2 cells complementary tests.

The viability of human bone marrow-derived MSCs after 1, 3, and 7 days of culture on the scaffold by Live/Dead staining (red, nonviable; green, viable; Fig. 7a), was evaluated.

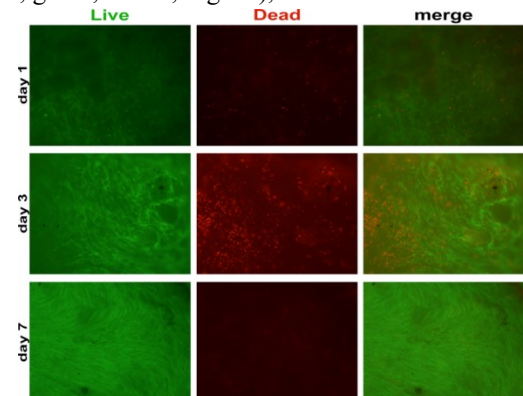


**Figure 7a.** Live&Dead assay. human MSCs cultured on HA-Coll-PCL scaffold. Representative images of fluorescence microscope micrographs showing MSCs on the top surface of the scaffold after 1, 3, and 7 days of culture in vitro. Live/dead cell assay was used to visualize live cells (calcein positive cells, in green) and dead cells (ethidium positive cells, in red).

MSCs adhered to the scaffold surface after 1 day of culture and most were viable, confirming the low toxicity of the material. At day 3 some dead cells, as well as cell spreading, were evident. At day 7 there were few dead cells, and the cells had formed a dense layer over most of the scaffold surface. No cells were detected beneath the surface of the scaffold.

To assess the effect of nHA-Coll-PCL on cell metabolism, an AB assay was performed at days 1, 3, and 7 of culture (Fig. 7b).

The MSCs on the scaffold were metabolically active. MSCs displayed significantly higher metabolic activity at days 3 and 7 compared to day 1. These data indicate that the scaffold has good biocompatibility: human MSCs adhered to and proliferated on the surface of the scaffold, and their metabolic activity was normal. The similarity of the XRD TEM, and BET results of natural bone and collagen fibers mineralized with nanosized HA,[6-18] may explain the biomimetic effect in terms of osteointegration, cell seeding, and formation of new bone. However the hydrophobic PCL could hamper differentiation of MSCs. In complementary tests, at 24 and 72 h, HePG2 and SAOS-2 cells exhibited growth on nHA-Coll and nHA-Coll-PCL (Fig. 8). To assess the effect of nHA-Coll-PCL on cell metabolism, an AB assay was performed at days 1, 3, and 7 of culture (Fig. 7b).

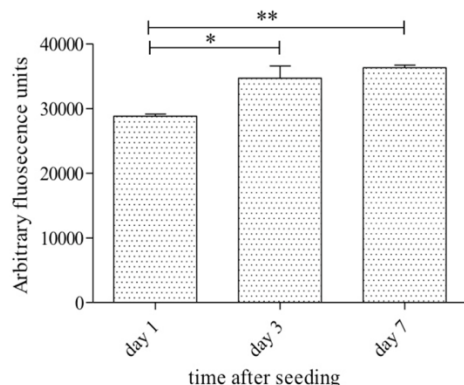


**Figure 7b.** Metabolic activity of human MSCs seeded on HA-Coll-PCL scaffold at days 1,3, and 7 of culture was evaluated by Alamar blue assay. Data represent mean values  $\pm$  SD of measurements obtained from three independent scaffolds. Each scaffold was assayed in duplicate; \* $p < 0.05$ ; \*\* $p < 0.01$ .

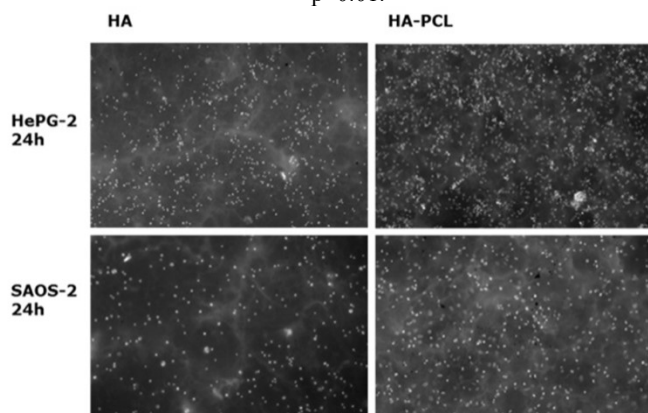


**Figure 8.** 4',6-Diamidine-2'-phenylindole dihydrochloride (DAPI) stained cells grown on tablets after 24 hours, imaged by fluorescent microscope using Neofluar objective 10X and a B/W camera (Zeiss Azio Imager M2).

The *in-vitro* part of this study showed no toxic residual element detected in the nHA-Coll-PCL material (LDH test). The

LDH cytotoxicity assay according to ISO 10993-5:2009 (part 5: Test for *in-vitro* cytotoxicity) and to ASTM E2526-08 showed no significant toxicity, even at the highest nHA-Coll-PCL concentration tested (50 mg/mL) (Fig. 9).

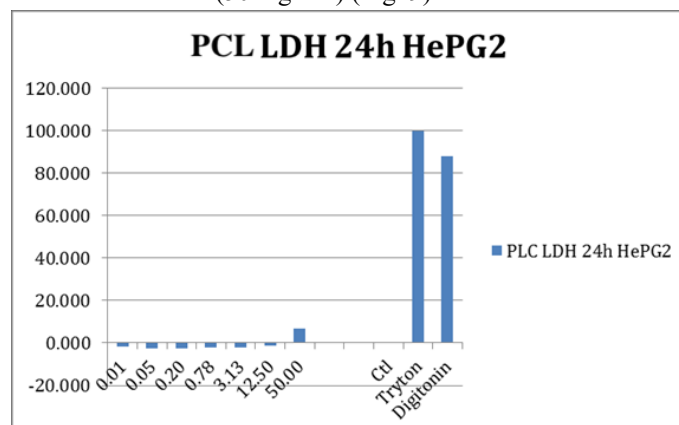


**Figure 9.** HePG2 cells were exposed to nHA-coll-PCL for 24 h. Results obtained by LDH assay performed on HePG2 cells, in accordance with ISO 10993-5:2009 (part 5: Tests for *in vitro* cytotoxicity) and ASTM E2526-08 (Standard Test Method for Evaluation of Cytotoxicity of Nanoparticulate Materials), showed there was no significant cytotoxicity even at the highest dose tested (50 mg/mL). Data are reported as % of cell death with respect to the untreated cells control ( $n=3$ ). 0.1% Tryton-X-100 as positive control and Digitonin (30  $\mu$ g/mL) as internal control have been included in the study.

### 3.2. *In vivo*.

In the *in-vivo* pilot test experiment, a digital process was used to customize the scaffold, and to prototype the bone plate to ensure that the primary stability was sufficient for osteointegration. The scaffold was fit precisely into the artificial bone defects using a surgical guide and an osteotomic oscillating saw. The customized bone plate stabilized the scaffold in the correct position to achieve the primary stability necessary for osteointegration. The artificial bone defect was restored with no complications during follow-up, and some areas showed new bone apposition at the external interface with the scaffold. (Fig. 10)

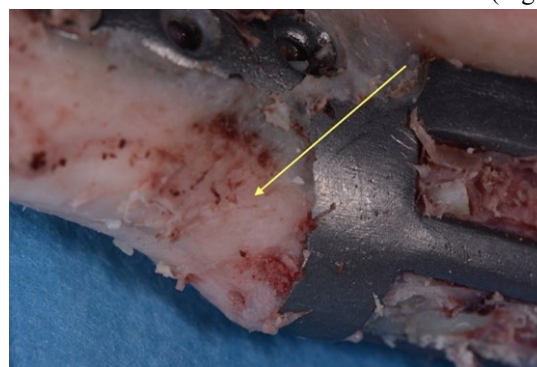


**Figure 10.** One of the areas with new bone apposition.

#### 3.2.1. Macroscopic analysis of the explanted specimen.

The explanted specimen appeared as a well-integrated material with good blood perfusion and no sign of inflammatory activity (granulomatous tissue, pus), confirming healing after the first (scaffold positioning) and second (oral implants insertion) surgeries.

In the distal area (toward the mandible gonium) (Fig. 10, arrow) a bony overcontouring of the bone plate was present in the area in which new calcific bone apposition was detected by micro-CT.



### 3.2.2. Micro-CT.

Micro-CT confirmed the continuity between the bone and the composite material, with no gap at the interface. Moreover, micro-CT revealed a zone of penetration of calcific bone in the distal wall of the inner scaffold (towards the mandibular gonion) (Fig. 11); other areas also showed seeding of mineralized bone tissue towards the core of the scaffold.

The newly formed bone started from the osteotomy lines and merged the material with the mandibular host bone.

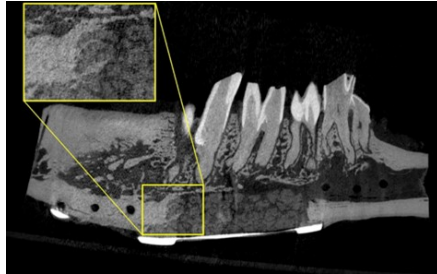


**Figure 11.** Microtomographic sagittal section of the sample with the zone of penetration of calcific bone at the inner material highlighted in the yellow inset.

### 3.2.3. Histological analysis.

Inflammatory cells were not detected around the graft, confirming its biocompatibility and the results of cytotoxicity tests that demonstrated an increasing level of metabolism of MSC on the surface of the composite material. Histological analysis revealed no adverse reaction at the interface between the implanted material and the host bone.

Most of the perimeter of the bone/scaffold interface was covered by a thin fibrous connective layer, while in other areas direct contact between the scaffold and the host bone indicated partial osteointegration and the biocompatibility of the implanted material (Fig. 12 a,b). In the areas where the material was in contact with the pre-existing bone no signs of resorption were present. These data confirm the micro-CT results.

Moreover, in other random areas of the inner scaffold, isolated aggregates of bone cells were detected (Fig. 13 a,b).

The histologic findings demonstrated the osteoinductive ability of the composite material; the presence of islands of bone cells in the inner scaffold may be due to random disaggregation of

the material, allowing penetration by blood clots. There was no living bone around implants at the inner portion of the scaffold.

The composite material was non-uniformly osteointegrated around the scaffold walls (Fig. 14 a,b blue arrows), which showed no seeding of bone tissue; the material is sufficiently inert and osseous-compatible for intimate contact with surrounding bone. A thin stratus of connective tissue was detected (Fig. 14a, yellow arrows) in some areas between the host bone and the scaffold. There was no osteointegration at the oral implant–scaffold interface, likely due to the absence of living bone in the inner scaffold.

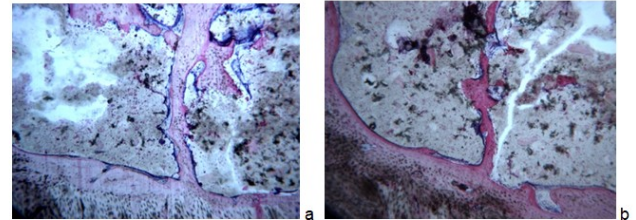


**Figure 12 (a,b).** Positive osteoinductive potential of the composite material.

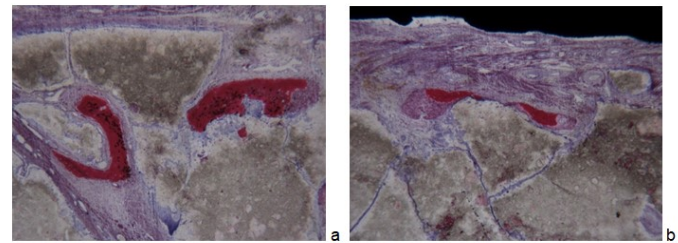


**Figure 13 (a,b).** Isolated islands of bone cells at the inner material.

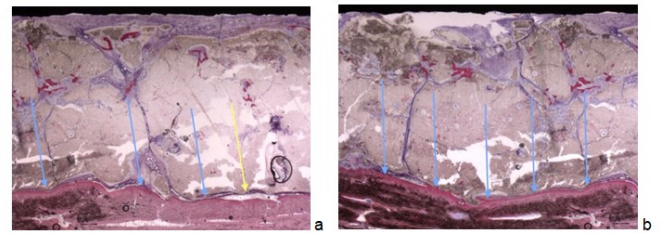


**Figure 14.** Osteointegration of the nHA-coll-PCL material at the interface (a-b, blue arrows) and areas of thin connective tissue layer (b, yellow arrows).

**Table 2.** Surface compositions of the HA samples.

Sample Identifier	Concentration (at%)					
	C	O	Ca	P	N	Ca/P
HA0 synthesized	14.38±0.3	55.69±0.03	18.52±0.03	11.36±0.39	nd	1.63
HA-coll	13.45±1.32	57.34±1.24	18.32±0.74	10.95±1.43	nd	1.67
HA-coll-PCL	45.2±1.53	39.10±1.06	9.7±0.45	6.61±0.61	nd	1.46
HA Theoretical [Ca <sub>10</sub> (PO <sub>4</sub> ) <sub>6</sub> (OH) <sub>2</sub> ]	--	61.9	23.81	14.3	--	1.66

## 4. CONCLUSIONS

The morphological analysis carried out by AFM and TEM showed a good homogeneity of the composite HA-coll-PCL. In particular, by TEM analysis, we have observed the mineralized fibers of collagen with nano HA. The XRD confirms a low crystallinity of the nano HA-coll present as a unique phase while XPS data exhibit the surface compositions of the samples showing a ratio Ca/P of 1.63, 1.67 and 1.47 for HA, HA/coll and HA/coll/PCL respectively. From AFM analysis we have obtained

interesting information about the adhesion and surface roughness values of the material useful to predict the behavior of the biomaterial in the biological system. BET analysis showed on HA-coll a value of the surface area of 127.27 m<sup>2</sup>/g: this value was very close to biogenic bone and all chemical–physical characterizations support the biomimetic approach used in the present work. The nHA-Coll-PCL composite material, because improved the surface propriety of the scaffold, showed good biocompatibility



and no cytotoxicity with human MSCs and complementary experimental cell lines (HePG2 and SAOS-2). Our hypothesis that improved hydrophilic properties of the scaffold and its bioactivity on surface might enhance the osteointegration with the surrounding bone and reduce the adverse inflammatory reactions, was confirmed. No inflammatory reaction was detected *in vivo*, and osteointegration was evident at the bone-scaffold interface in

several areas. The material was not resorbed, but some areas showed external apposition of new bone and cell seeding in the inner scaffold, with isolated agglomerates of living bone randomly distributed deep within the scaffold. Future studies are needed to develop a new physical composition of this material for the direct 3D printing of the scaffold.

## 5. REFERENCES

- Noetzel, J.; Kielbassa, A.M. Calcium phosphate cements in medicine and dentistry--a review of literature. *Schweiz Monatsschr Zahnmed* **2005**, *115*, 1148–1156.
- Götz, W.; Gerber, T.; Michel, B.; Lossdörfer, S.; Henkel, K.O.; Heinemann, F. Immunohistochemical characterization of nanocrystalline hydroxyapatite silica gel (NanoBone(r)) osteogenesis: a study on biopsies from human jaws. *Clin Oral Implants Res.* **2008**, *19*, 1016–1026, <https://doi.org/10.1111/j.1600-0501.2008.01569.x>.
- Canullo, L.; Heinemann, F.; Gedrange, T.; Biffar, R.; Kunert-Keil, C. Histological evaluation at different times after augmentation of extraction sites grafted with a magnesium-enriched hydroxyapatite: double-blinded randomized controlled trial. *Clin Oral Implants Res.* **2013**, *24*, 398–406, <https://doi.org/10.1111/clr.12035>.
- Kunert-Keil, C.; Götz, W.; Heinemann, F. Implants, bone and soft tissues—An international update 2015. *Ann Anat.* **2015**, *199*, 1–2, <https://doi.org/10.1016/j.aanat.2015.04.001>.
- Guda, T.; Appleford, M.; Oh, S.; Ong, J.L. A cellular perspective to bioceramic scaffolds for bone tissue engineering: the state of the art. *Curr Top Med Chem* **2008**, *8*, 290–299, <https://doi.org/10.2174/156802608783790956>.
- Rnjak-Kovacina, J.; Weiss, A.S. Increasing the pore size of electrospun scaffolds. *Tissue Eng. B Rev.* **2011**, *17*, 365–372, <https://doi.org/10.1089/ten.teb.2011.0235>.
- Lotfi, M.; Bagherzadeh, R.; Naderi-Meshkin, H.; Mahdipour, E.; Mafinezhad, A.; Sadeghnia, H.R.; Esmaily, H.; Maleki, M.; Hassanzadeh, H.; Ghayaour-Mobarhan, M.; Bidkhor, H.R.; Bahrami, A.R. Hybrid chitosan-ss-glycerol phosphate-gelatin nano-/micro fibrous scaffolds with suitable mechanical and biological properties for tissue engineering. *Biopolymers* **2016**, *105*, 163–175.
- Hollister, S.J.; Maddox, R.D.; Taboasa, J.M. Optimal design and fabrication of scaffolds to mimic tissue properties and satisfy biological constraints. *Biomaterials* **2002**, *23*, 4095–4103, [https://doi.org/10.1016/S0142-9612\(02\)00148-5](https://doi.org/10.1016/S0142-9612(02)00148-5).
- Cunha, C.; Panseri, S.; Sandri, M.; Maracchi, M.; Tampieri, A. Inspired by nature. *Mater Today* **2012**, *15*, 223–228.
- Iafisco, M.; Sabatino, P.; Lesci, I.G.; Prat, M.; Rimondini, L.; Roveri, N. Conformational modifications of serum albumins adsorbed on different kinds of biomimetic hydroxyapatite nanocrystals. *Colloids Surf B: Biointerfaces* **2010**, *8*, 274–284, <https://doi.org/10.1016/j.colsurfb.2010.07.022>.
- Nelson, C.; Khan, Y.; Laurencin, C.T. Nanofiber-microsphere (nano-micro)matrices for bone regenerative engineering: a convergence approach toward matrix design. *Regenerative Biomater.* **2014**, *1*, 3–9, <https://doi.org/10.1093/rb/rbu002>.
- Yang, C.X.; Gao, C.; Wan, Y.Z.; Tang, T.T.; Zhang, S.H.; Dai, K.R. Preparation and characterization of three-dimensional nanostructured macroporous bacterial cellulose/ agarose scaffold for tissue engineering. *J Porous Mater.* **2011**, *18*, 545–552, <https://doi.org/10.1007/s10934-010-9407-z>.
- Kubasiewicz-Ross, P.; Hadzik, J.; Seeliger, J.; Kozak, K.; Jarczyszyn, K.; Gerber, H.; Dominiak, M.; Kunert-Keil, C. New nano-hydroxyapatite in bone defect regeneration: A histological study in rats. *Ann Anat.* **2017**, *213*, 83–90, <https://doi.org/10.1016/j.aanat.2017.05.010>.
- Garagiola, U.; Grigolato, R.; Soldo, R.; Bacchini, M.; Bassi, G.; Roncucci, R.; De Nardi, S. Computer-aided design/computer-aided manufacturing of hydroxyapatite scaffolds for bone reconstruction in jawbone atrophy: a systematic review and case report. *Maxillofac Plast Reconstr Surg.* **2016**, *4*, 38–42, <https://doi.org/10.1186/s40902-015-0048-7>.
- Teotia, A.K.; Raina, D.B.; Singh, C.; Sinha, N.; Isaksson, H.; Tägil, M.; Lidgren, L.; Kumar, A. Nano-hydroxyapatite bone substitute functionalized with bone active molecules for enhanced cranial bone regeneration. *ACS Appl Mater Interfaces.* **2017**, *9*, 6816–6828, <https://doi.org/10.1021/acsami.6b14782>.
- Kim, I.G.; Hwang, M.P.; Du, P.; Ko, J.; Ha, C.W.; Do, S.H.; Park, K. Bioactive cell-derived matrices combined with polymer mesh scaffold for osteogenesis and bone healing. *Biomaterials* **2015**, *50*, 75–86, <https://doi.org/10.1016/j.biomaterials.2015.01.054>.
- Xu, W.; Wang, A.; Lu, A. Cartilage ECM-derived 3-D porous acellular matrix scaffold for *in vivo* cartilage tissue engineering with PKH26-labeled chondrogenic bone marrow-derived mesenchymal stem cells. *Biomaterials* **2008**, *29*, 2378–2387.
- Ciocca, L.; Lesci, I.G.; Mezini, O.; Parrilli, A.; Ragazzini, S.; Rinnovati, R.; Romagnoli, N.; Roveri, N.; Scotti, R. Customized hybrid biomimetic hydroxyapatite scaffold for bone tissue regeneration. *J Biomed Mater Res B Appl Biomater.* **2017**, *105*, 723–734, <https://doi.org/10.1002/jbm.b.33597>.
- Meng, S.; Zhang, Z.; Rouabhia, M. Accelerated osteoblast mineralization on a conductive substrate by multiple electrical stimulation. *Journal of Bone and Mineral Metabolism* **2011**, *29*, 535–544, <https://doi.org/10.1007/s00774-010-0257-1>.
- Dorozhkin, S.V. Bioceramics of calcium orthophosphates. *Biomaterials* **2010**, *31*, 1465–1485, <https://doi.org/10.1016/j.biomaterials.2009.11.050>.
- Pierini, M.; Dozza, B.; Lucarelli, E.; Tazzari, P.L.; Ricci, F.; Remondini, D.; Di Bella, C.; Giannini, S.; Donati, D. Efficient isolation and enrichment of mesenchymal stem cells from bone marrow. *Cytotherapy* **2012**, *14*, 686–672, <https://doi.org/10.3109/14653249.2012.677821>.
- Zhou, X.; Holsbeeks, I.; Impens, S.; Sonnaert, M.; Bloemen, V.; Luyten, F.; Schrooten, J. Noninvasive real-time monitoring by alamarBlue(®) during *in vitro* culture of three-dimensional tissue-engineered bone constructs. *Tissue Eng Part C Methods* **2013**, *19*, 720–729, <https://doi.org/10.1089/ten.TEC.2012.0601>.
- Piattelli, A.; Piattelli, M.; Scarano, A. Simultaneous demonstration of alkaline and acid phosphatase activity in bone, at bone-implant interfaces and at the epiphyseal growth plate in plastic-embedded undemineralized tissues. *Biomaterials* **1997**, *18*, 545–549, [https://doi.org/10.1016/S0142-9612\(96\)00172-X](https://doi.org/10.1016/S0142-9612(96)00172-X).
- De Lange, G.L.; Overman, J.R.; Farre-Guasch, E.; Korstjens, C.M.; Hartman, B.; Langenbach, G.E.; Van Duin, M.A.; Klein-Nulend, J. A histomorphometric and micro-computed

tomography study of bone regeneration in the maxillary sinus comparing biphasic calcium phosphate and deproteinized cancellous bovine bone in a human split-mouth model. *Oral Surg Oral Med Oral Pathol Oral Radiol.* **2014**, *117*, 117-125, <https://doi.org/10.1016/j.oooo.2013.08.008>.

25. Haimi, S.; Suuriniemi, N.; Haaparanta, A.M. *et al.* Growth and osteogenic differentiation of adipose stem cells on PLA/bioactive glass and PLA/ $\beta$ -TCP scaffolds. *Tissue Eng Part A.* **2009**, *15*, 1473-1481, <https://doi.org/10.1089/ten.tea.2008.0241>.

26. Li, J.; Hsu, Y.; Luo, E.; Khadka, A.; Hu, J. Computer-aided design and manufacturing and rapid prototyped nanoscale hydroxyapatite/polyamide (n-HA/PA) construction for condylar defect caused by mandibular angle osteotomy. *Aesthetic Plast Surg.* **2011**, *35*, 636-642, <https://doi.org/10.1007/s00266-010-9602-y>.

27. Meseguer-Olmo, L.; Vicente-Ortega, V.; Alcaraz-Banos, M.; Calvo-Guirado, J.L.; Vallet-Regí, M.; Arcos, D.; Baeza, A. *In vivo* behavior of Si-hydroxyapatite /polycaprolactone/DMB scaffolds fabricated by 3D printing. *J Biomed Mater Res A.* **2013**, *101*, 2038-2046, <https://doi.org/10.1002/jbm.a.34511>.

28. Mesimäki, K.; Lindroos, B.; Tornwall, J.; Mauno, J.; Lindqvist, C.; Kontio, R.; Miettinen, S.; Suuronen, R. Novel maxillary reconstruction with ectopic bone formation by GMP adipose stem cells. *Int J Oral Maxillofac Surg.* **2009**, *38*, 201-209, <https://doi.org/10.1016/j.jom.2009.01.001>.

29. Rohner, D.; Huttmacher, D.W.; Cheng, T.K.; Oberholzer, M.; Hammer, B. *In vivo* efficacy of bone-marrow-coated polycaprolactone scaffolds for the reconstruction of orbital defects in the pig. *J Biomed Mater Res B Appl Biomater.* **2003**, *66*, 574-582, <https://doi.org/10.1002/jbm.b.10037>.

30. Salgado, A.J.; Coutinho, O.P.; Reis, R.L. Bone-tissue engineering: State of the art and future trends. *Macromol Biosci.* **2004**, *4*, 743-751, <https://doi.org/10.1002/mabi.200400026>.

31. Xu, H.; Han, D.; Dong, J.S.; Shen, G.X.; Chai, G.; Yu, Z.Y.; Lang, W.J.; Ai, S.T. Rapid prototyped PGA/PLA scaffolds in the reconstruction of mandibular condyle bone defects. *Int J Med Robot.* **2010**, *6*, 66-74, <https://doi.org/10.1002/rcs.290>.

32. Alonso-Rodríguez, E.; Cebrian, J.L.; Nieto, M.J.; Del Castillo, J.L.; Hernandez-Godoy, J.; Burgueno, M. Polyetheretherketone custom-made implants for craniofacial defects: report of 14 cases and review of the literature. *J Craniomaxillofac Surg.* **2015**, *43*, 1232-1238, <https://doi.org/10.1016/j.jcms.2015.04.028>.

33. O'Reilly, E.B.; Barnett, S.; Madden, C.; Welch, B.; Mickey, B.; Rozen, S. Computed tomography modeled polyether ether ketone (PEEK) implants in revision cranioplasty. *J Plast Reconstr Aesthet Surg.* **2015**, *68*, 329-338, <https://doi.org/10.1016/j.bjps.2014.11.001>.

34. Ciocca, L.; Donati, D.; Ragazzini, S.; Dozza, B.; Rossi, F.; Fantini, M.; Spadari, A.; Romagnoli, N.; Landi, E.; Tampieri, A.; Piattelli, A.; Lezzi, G.; Scotti, R. Mesenchymal stem cells and platelet gel improve bone deposition within CAD-CAM custom-made ceramic HA scaffolds for condyle substitution.

*Biomed Res Int.* **2013**, *2013*, 549762, <https://doi.org/10.1155/2013/549762>.

35. Ciocca, L.; Donati, D.; Fantini, M.; Landi, E.; Piattelli, A.; Lezzi, G.; Tampieri, A.; Spadari, A.; Romagnoli, N.; Scotti, R. CAD-CAM-generated hydroxyapatite scaffold to replace the mandibular condyle in sheep: preliminary results. *J Biomater Appl.* **2013**, *28*, 207-218, <https://doi.org/10.1177/0885328212443296>.

36. Eighmy, T.T.; Kinner, A.E. Hinsdalite (PbAl<sub>3</sub>PO<sub>4</sub>SO<sub>4</sub>(OH)<sub>6</sub>) Characterized by XPS: An Environmentally Important Secondary Mineral. *Surface Science Spectra* **1999**, *6*, 184-192, <https://doi.org/10.1116/1.1247928>.

37. Ciocca, L.; De Crescenzo, F.; Fantini, M.; Scotti, R. CAD/CAM and rapid prototyped scaffold construction for bone regenerative medicine and surgical transfer of virtual planning: a pilot study. *Comput Med Imaging Graph.* **2009**, *33*, 58-62, <https://doi.org/10.1016/j.compmedimag.2008.10.005>.

38. Lesci, I.G.; Ciocca, L.; Roveri, N. Biomimetic customized composite scaffolds and translational models for the bone regenerative medicine using CAD-CAM technology. In: *Handbook of Bioceramics and Biocomposites*. 2016; pp. 585-613, [https://doi.org/10.1007/978-3-319-12460-5\\_28](https://doi.org/10.1007/978-3-319-12460-5_28).

39. Del Bianco, L.; Lesci, I.G.; Fracasso, G.; Barucca, G.; Spizzo, F.; Tamisari, M.; Scotti, R.; Ciocca, L. Synthesis of nanogranular Fe<sub>3</sub>O<sub>4</sub>/biomimetic hydroxyapatite for potential applications in nanomedicine: Structural and magnetic characterization. *Mat Res Express.* **2015**, *2*.

40. Beamson, P.; Briggs, D. (eds), *High Resolution XPS of Organic Polymers – The Scienta ESCA300 Database*. Wiley, 1992; <https://doi.org/10.1021/ed070pA25.5>.

41. Torres-Lagares, D.; Castellanos-Cosano, L.; Serrera-Figallo, M.Á.; García-García, F.J.; López-Santos, C.; Barranco, A.; Rodríguez-Gonzalez, Elise, A.; Rivera-Jiménez, C.; Gutiérrez-Pérez, J.L. In Vitro and in Vivo Study of Poly(Lactic-co-Glycolic) (PLGA) Membranes Treated with Oxygen Plasma and Coated with Nanostructured Hydroxyapatite Ultrathin Films for Guided Bone Regeneration Processes. *Polymers* **2017**, *9*, 410-417, <https://doi.org/10.3390/polym9090410>.

42. Lesci, I.G.; Ciocca, L.; Mezini, O.; Roveri, N. Synthetic biomimetic HA composite scaffolds for bone regenerative medicine using CAD-CAM technology. *Key Engineer Mat.* **2015**, *672*, 235-246, <https://doi.org/10.4028/www.scientific.net/KEM.672.235>.

43. Ciocca, L.; Donati, D.; Lesci, I.G.; Dozza, B.; Duchi, S.; Mezini, O.; Spadari, A.; Romagnoli, N.; Scotti, R.; Roveri, N. Custom-made novel biomimetic composite scaffolds for bone regenerative medicine. *Mat Lett.* **2014**, *136*, 393-396, <https://doi.org/10.1016/j.matlet.2014.08.097>.

44. Ciocca, L.; Lesci, I.G.; Mezini, O.; Parrilli, A.; Ragazzini, S.; Rinnovati, R.; Romagnoli, N.; Roveri, N.; Scotti, R. Customized hybrid biomimetic hydroxyapatite scaffold for bone tissue regeneration. *J Biomed Mater Res B Appl Biomater.* **2017**, *105*, 723-734, <https://doi.org/10.1002/jbm.b.33597>.

## 6. ACKNOWLEDGEMENTS

Authors thanks dr. Andrea Sandi for his valuable work during CAD-CAM process. The English in this document has been checked by at least two professional editors, both native speakers of English. For a certificate, please see: <http://www.textcheck.com/certificate/E9n2pG>. This research did not receive any specific grant from funding agencies in the public, commercial, or not-for-profit sectors. The investigations were carried out following the rules of the Declaration of Helsinki of 1975 (<https://www.wma.net/what-we-do/medical-ethics/declaration-of-helsinki/>), revised in 2013. All animal tests described in this paper were carried out in accordance with the EU Directive 2010/63/EU for animal experiments. All operations and treatments were carried out by veterinarians, and animal boarding management was carried out by veterinarians and animal health technicians. The study was approved by the Ethics Board of the Italian National Institute of Health (no. 781/2015-PR).



© 2020 by the authors. This article is an open access article distributed under the terms and conditions of the Creative Commons Attribution (CC BY) license (<http://creativecommons.org/licenses/by/4.0/>).